

Intertwined Spin and Orbital Density Waves in MnP Uncovered by Resonant Soft X-Ray Scattering

B. Y. Pan,^{1,2} H. Jang,³ J.-S. Lee,³ R. Sutarto,⁴ F. He,⁴ J. F. Zeng,^{5,6} Y. Liu,⁷ X. W. Zhang,¹ Y. Feng,¹
Y. Q. Hao,¹ J. Zhao,^{1,8} H. C. Xu,¹ Z. H. Chen,⁹ J. P. Hu,^{5,10,11,*} and D. L. Feng^{1,8,†}

¹*State Key Laboratory of Surface Physics, Department of Physics, and Advanced Materials Laboratory, Fudan University, Shanghai 200433, China*

²*School of Physics and Optoelectronic Engineering, Ludong University, Yantai, Shandong 264025, China*

³*Stanford Synchrotron Radiation Lightsource, SLAC National Accelerator Laboratory, Menlo Park, California 94025, USA*

⁴*Canadian Light Source, Saskatoon, Saskatchewan S7N 2V3, Canada*

⁵*Beijing National Laboratory for Condensed Matter Physics, and Institute of Physics, Chinese Academy of Sciences, Beijing 100190, China*

⁶*University of Chinese Academy of Sciences, Beijing 100049, China*

⁷*Center for Correlated Matter, Zhejiang University, Hangzhou, 310058, China*

⁸*Collaborative Innovation Centre of Advanced Microstructures, Nanjing 210093, China*

⁹*Shanghai Institute of Applied Physics, Chinese Academy of Sciences,*

Shanghai Synchrotron Radiation Facility, Shanghai 201800, China

¹⁰*Kavli Institute of Theoretical Sciences, University of Chinese Academy of Sciences, Beijing, 100190, China*

¹¹*Collaborative Innovation Center of Quantum Matter, Beijing 100084, China*

 (Received 22 February 2019; revised manuscript received 2 May 2019; published 19 June 2019)

Unconventional superconductors are often characterized by numerous competing and even intertwined orders in their phase diagrams. The fluctuations associated with these orders may provide the exotic pairing glue that underlies their high-temperature superconductivity. Helimagnet MnP, the first Mn-based superconductor under pressure, lacks high rotational symmetry. However, our resonant soft x-ray scattering experiment discovers novel helical orbital density wave (ODW) orders in MnP and reveals intertwined ordering phenomena. In particular, an ODW forms with half the period of the spin order and fully develops slightly above the spin ordering temperature, which resembles the behaviors of the nematic phase of the iron-based superconductors. Moreover, we find that their domains develop simultaneously, yet the spin order domains are larger than those of the ODW; and they cooperatively produce another ODW with 1/3 the period of the spin order. These observations provide a comprehensive picture of the intertwined orders in this three-dimensional, low-symmetry system and shed light on the understanding of its superconducting mechanism.

DOI: [10.1103/PhysRevX.9.021055](https://doi.org/10.1103/PhysRevX.9.021055)

Subject Areas: Condensed Matter Physics,
Strongly Correlated Materials

In strongly correlated electron systems, the kinetic and interaction energies of electrons compete, which often couples the charge, spin, and orbital degrees of freedoms, resulting in a variety of complex quantum phases. For example, the stripe phase in the cuprate contains both spin and charge orders, while the nematic phase in iron-based

superconductors, which spontaneously break rotational symmetry, involve both spin and orbital orders [1–4]. The nature of the ordering in the parent phases of unconventional superconductors may contain crucial information on superconductivity. For example, the orbital and/or spin fluctuations associated with the nematic phase are suggested to promote superconductivity in iron pnictides [5,6].

Manganese phosphide (MnP) is a helimagnet with rich phases and intriguing properties such as the topological Hall effect (THE) [7]. In particular, it has been recently found to be the first Mn-based superconductor under pressure [8]. At an ambient pressure, MnP first enters a ferromagnetic state at $T_C = 290$ K, and then a metamagnetic transition at $T_S = 50$ K switches it into a

*jphu@iphy.ac.cn

†dlfeng@fudan.edu.cn

Published by the American Physical Society under the terms of the Creative Commons Attribution 4.0 International license. Further distribution of this work must maintain attribution to the author(s) and the published article's title, journal citation, and DOI.

double-helical magnetic state with moments lying in the *ab* plane [Figs. 1(a) and 1(b)]. Such a complex magnetic behavior suggests that MnP is most likely an unconventional superconductor like the cuprate and iron pnictides. However, not only has the material a helical magnetic state that differs from those of cuprates and iron-based superconductors [Fig. 1(b)], but its lattice structure is three dimensional and does not possess any high-symmetry rotational axis. Moreover, since the spin, charge, and orbital degrees of freedom could be highly interconnected in MnP, it provides a novel playground to probe the interplay between various orderings in a low-symmetry three-dimensional system, in contrast to the quasi-two-dimensional square lattices of cuprates and iron-based

superconductors. Here, we report the resonant x-ray scattering studies on MnP. The results reveal novel orbital density wave (ODW) orders and their interesting interplay with the spin density wave (SDW). Especially, an ODW order at q_2 is half the periodicity of the SDW, and its fully developed temperature is slightly above that of the SDW. These two features resemble the behaviors of the nematic orbital order in iron-based superconductors. For example, in LaFeAsO and BaFe_{2-x}Co_xAs₂ [9–11], the orbital order often emerges at a higher temperature than the collinear antiferromagnetic order, and with half the period, indicating that the nematicity may be strongly tied to magnetic fluctuations. Similarly, in the stripe phase of the cuprates, the charge order forms with half the period of the spin order

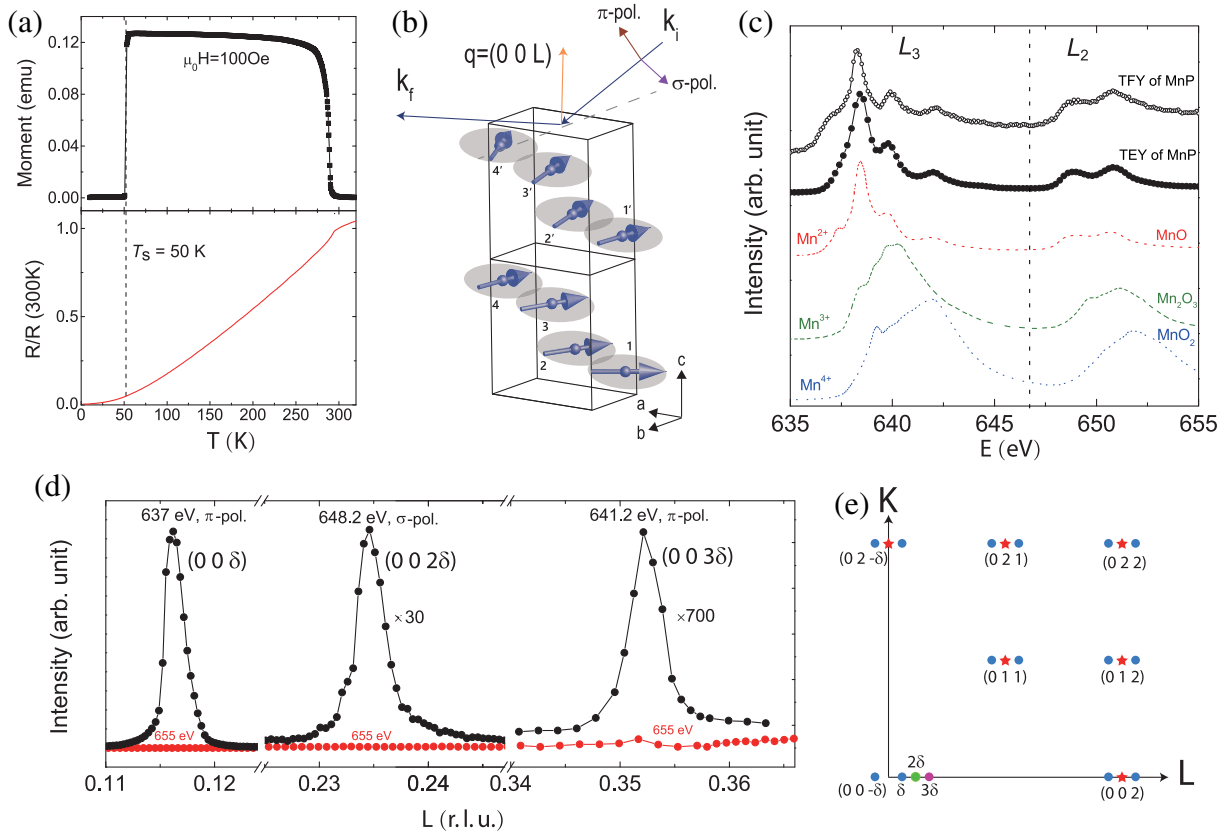


FIG. 1. Basic properties and x-ray diffraction peaks of MnP. (a) Magnetic susceptibility and resistance data of the MnP single-crystal sample. (b) Schematic illustration of the helical spin order and the RIXS scattering geometry. The spin rotates about 21° between Mn1 and Mn2, and between Mn3 and Mn4, giving an incommensurate double helical spin order, or a helical spin density wave (SDW), with a period of about $8.6c$. Mn1 and Mn3 spins form one spin helix, and Mn2 and Mn4 spins form the other. The incident x ray is linearly polarized. (c) X-ray absorption spectroscopy (XAS) of MnP (solid black dots) and three reference compounds MnO (dashed red line), Mn₂O₃ (dashed olive line), and MnO₂ (dashed blue line) around the Mn *L* edge. The reference spectra are obtained on beam line 8.0.3 at the Advanced Light Source [14] and are plotted here offset by 1.55 eV in order to match our MnP spectrum obtained at the SSRL. The Mn *L*-edge XAS of MnP is characteristic of Mn²⁺ ions. The hollowed black dots represent the bulk sensitive total fluorescence yield (TFY) spectra of MnP which is simultaneously measured with the TEY spectra. (d) Scattering peaks around $q_1 = (000.116)$ r.l.u., $q_2 = (000.234)$ r.l.u., and $q_3 = (000.352)$ r.l.u. at resonant energies (black dots) and nonresonant energy (red dots, $E = 655$ eV) at 20 K. q_1 and q_2 signals are measured by a Schottky barrier photodiode, and the q_3 signals are measured by a quantum-efficient channeltron. The three resonant peaks represent the strongest resonant signals at each q position (see Fig. 3). (e) Schematic diagram of the location of the diffraction peaks in MnP including lattice peaks (red stars), magnetic peaks (blue dots), and the newly discovered resonance peaks in this paper (green and magenta dots).

[12,13]. The common features among orders of MnP and those of the cuprate and iron-based superconductors, together with the ubiquitous presence of competition between ordered phases and superconducting phases, highlight a unified theme of these unconventional superconductors, which sheds light on the understanding of their superconducting mechanisms.

Resonant soft x-ray scattering (RSXS), which can be viewed as a combination of x-ray absorption (XAS) and x-ray emission spectroscopies with x-ray scattering, provides a direct and powerful probe of the ordering in $3d$ transition metal compounds [15–17]. To elucidate the electronic state of MnP, we first present its XAS spectrum measured by the total electron yield (TEY) at the Mn L edge in Fig. 1(c), together with that of MnO as a fingerprint of the Mn^{2+} valence state [14], Mn_2O_3 as a typical Mn^{3+} spectrum, and MnO_2 representing Mn^{4+} . The bulk sensitive total fluorescence yield (TFY) of MnP [hollowed black dots in Fig. 1(c)] is simultaneously measured. Both its TEY and TFY spectra consistent with the Mn^{2+} spectrum, the multiplet features in the pre- and postedge can be well interpreted by the transition processes from the $2p^63d^5$ ground state to a series of $2p^53d^6$ final states [18,19]. So the resonant scatterings at the Mn L edge should involve only orderings of the Mn $3d$ electrons. The combination of TEY and TFY excludes extrinsic artifacts such as oxidation or degradation on the surface. We also perform an x-ray photoemission spectroscopy measurement for the experimental sample, confirming a clean surface (Fig. S2 in Supplemental Material [20]). Evidently, MnP has the typical absorption spectrum of a Mn^{2+} state with the half filling high spin configuration. To our knowledge, this is the first XAS measurement on MnP. The Mn^{2+} state in MnP is contrary to the previously speculated $\text{Mn}^{3+}\text{P}^{3-}$ [21] or $\text{Mn}^{1+}\text{P}^{1-}$ [22] valence state in this material. The spin moment on each Mn site is only about $1.3\mu_B$ [23]; this value is significantly reduced from the localized spin-only moment of about $5\mu_B$ for the $3d^5$ configuration in Mn^{2+} by Hund's rule. This low spin moment may arise from quantum fluctuations and hybridization [24,25], as is the case for the iron-based superconductors [26,27]. It should be noted that for a half filled electronic system, the orbital moment usually is quenched, thus prohibiting spin-orbital coupling. However, orbital anisotropy or ordering has been found in several half filled systems due to hybridization anisotropy [28] and vacancy modulation [29]. Therefore, orbital angular momentum may be partially restored.

Figure 1(b) shows the scattering geometry, where the bc crystal plane is used as the scattering plane. The incident x ray is either horizontally (π) or vertically (σ) polarized to the scattering plane. In this configuration, σ polarization has an electric field along the a axis and momentum transfer along the $(0\ 0\ L)$ direction. When helical magnetic order emerges below $T_S = 50$ K, its spin moments (blue arrows) lie in the ab plane with magnetic propagation wave

vector $q_m = (000.117)$ [30]. In order to avoid specular reflection, we use a MnP single crystal with a $(1\ 0\ 1)$ surface and tilt the sample by 48.4° in our RSXS experiments. Detailed experimental settings are described in Supplemental Material [20].

We make an exhaustive search for scattering signals at the Mn L edge along $(0\ 0\ L)$ at 20 K. By varying L , x-ray polarization, photon energy, and detection mode, we discover resonance peaks at $q_1 = (000.11634 \pm 0.00002)$ r.l.u., $q_2 = (000.23470 \pm 0.00003)$ r.l.u., and $q_3 = (000.35239 \pm 0.00004)$ r.l.u. q_2 and q_3 wave vectors approximately double and triple that of q_1 , respectively. Figure 1(d) shows the scans for the strongest resonance peaks at q_1 ($E = 637$ eV, π polarization, black dots), q_2 ($E = 648.2$ eV, σ polarization, black dots), q_3 ($E = 641.2$ eV, π polarization, black dots), and the corresponding nonresonant scans at 655 eV (red dots). q_1 is perfectly consistent with the magnetic diffraction peak at q_m in MnP. As a helimagnet, there should be no higher-order magnetic diffractions in MnP [31,32]. However, the presence of a spin bunching distortion could produce additional higher odd-order diffractions [33]. More interestingly, a recent neutron study reports the observation of second- and third-order diffractions whose origin is to be investigated [34]. To elucidate the nature of the q_2 and q_3 resonant diffractions, a comprehensive study by RSXS is necessary. In Fig. 1(e), we illustrate the diffraction positions of the lattice, the first-order and higher-order diffractions discovered by our RSXS measurements in reciprocal space.

Next, we study the temperature dependencies of the diffraction peaks. First, we take the $(0\ 0\ 2)$ lattice diffraction peak as a reference. It does not show any observable temperature dependence across T_S and down to 20 K [Fig. 2(a)], indicating no structure transition in this temperature range. In contrast, q_1 , q_2 , and q_3 peaks exhibit drastic temperature dependencies. Figures 2(b)–2(d) show the three diffraction peaks taken with their corresponding resonant scattering conditions, at q_1 ($E = 637$ eV, π polarization), q_2 ($E = 648.8$ eV, π polarization), and q_3 ($E = 636.6$ eV, π polarization) at different temperatures in a cooling sequence, respectively. As can be seen, not only does the peak intensity rapidly grow across T_S , but the propagation wave vector moves to higher q with a decreasing temperature. The peak areas of the q_1 , q_2 , and q_3 diffraction peaks are plotted as a function of the temperature in Fig. 2(e), all showing a jump just around 50 K, consistent with a first-order transition [the hysteresis behavior of the q_1 peak can be found in Supplemental Fig. S5(a) [20]]. Interestingly, the q_1 peak is fully developed at a slightly lower temperature than the q_2 peak, while the full-development temperature of the q_3 peak lies in between or similar to the q_2 peak. This observation can be justified by more temperature dependence measurements [Supplemental Fig. S5(b) [20]]. In Fig. 2(f), we show the wave vector evolution with the

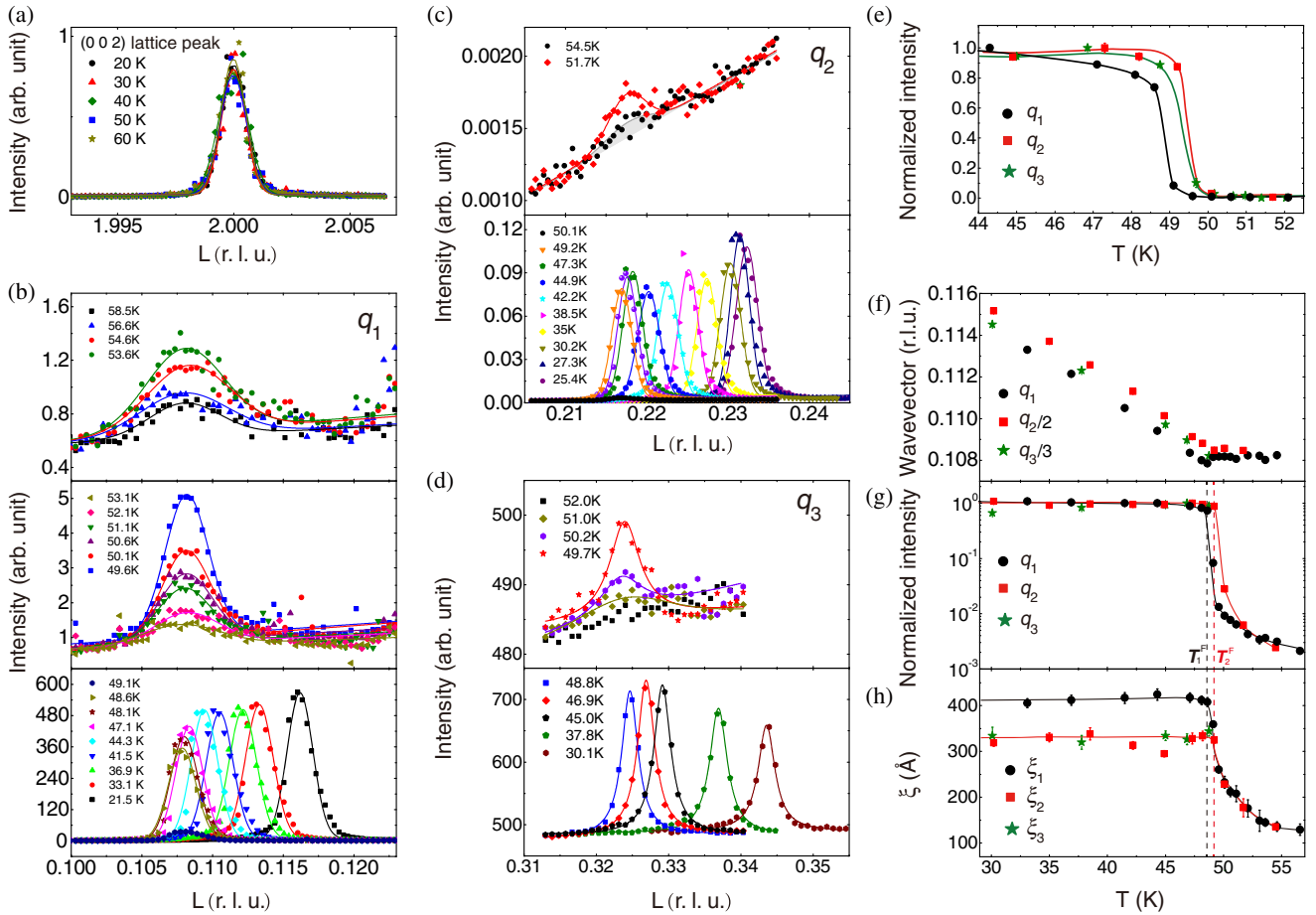


FIG. 2. Temperature dependencies of the diffractions peaks in MnP. (a) (0 0 2) lattice peak measured at 2180 eV from 20 to 60 K. (b)–(d), q_1 L_3 ($E = 637$ eV, π polarization), q_2 L_2 ($E = 648.8$ eV, π polarization), and q_3 L_3 ($E = 636.6$ eV, π polarization) resonance peaks at different temperatures, measured on cooling. The solid lines in each panel are Gaussian (for q_1 and q_2 resonance peaks) or Lorentz (for q_3 resonance peaks) fittings with a linear background. The shadowed area in the upper panel in (c) is to indicate the weak peak intensity at the highest measured temperature. (e) Temperature dependence of the peak area of q_1 , q_2 , and q_3 near the helical transition, revealing their differing transition temperatures. The data are obtained in the cooling processes. Solid lines are guides to the eye. (f) Temperature dependences of the q_1 , $q_2/2$, and $q_3/3$. Here, we use a photodiode detector for q_1 , a channeltron detector for q_2 , and a Greateyes CCD for q_3 . (g) and (h) are the temperature dependences of the peak area and $1/\text{FWHM}$ for q_1 (black circles) and q_2 (red squares) resonance peaks in the cooling measurements, respectively. (g) and (e) display the same set of data but use different scales. In (g), the log scale is used for the vertical axis in order to reveal the detailed high-temperature evolution. The solid lines are guides to the eye.

temperature, in which q_2 and q_3 are divided by 2 and 3, respectively, in order to scale with q_1 . The propagation wave vectors of the three resonance peaks all show pronounced temperature dependence below T_S , which is typical for an incommensurate electronic order. Throughout the measured temperature range, q_2 and q_3 are approximately at the $2q_1$ and $3q_1$ positions within the experimental accuracy, respectively, indicating that these electronic orders are interconnected with each other. According to the upper panels in Figs. 2(b)–2(d), there are detectable scattering intensities above T_S . The q_1 and q_2 peaks persist up to the highest measured temperatures, i.e., 58.5 and 54.5 K, respectively [upper panels in Figs. 2(b) and 2(c)]. However, q_3 peak intensity is not detectable above 52 K [upper panel in

Fig. 2(d)] due to its weak intensity and insufficient sensitivity of the detector. To reveal the detailed evolution at high temperatures, in Fig. 2(g), we plot the cooling data of peak areas in the log scale for the vertical axis. Figure 2(h) shows the temperature dependence of the correlation length, ξ_i , which is defined as $1/\text{FWHM}$, reflecting the average domain size along c . Above 50 K, there is a similar slow-growing behavior for both the q_1 and q_2 peaks in Figs. 2(g) and 2(h). The peak intensities are 2 orders of magnitude lower than their full values; thus, they are due to fluctuating orders, and the long tails into high temperatures are likely related to local strain distributions. A similar behavior is observed for the nematic order in iron pnictides under uniaxial strain [10]. With a decreasing temperature, ξ_1 and ξ_2 quickly increase

almost identically before they saturate at T_1^F and T_2^F , respectively, indicating the peaks are from the same domain and have the same onset temperature T^E , which can be higher than 58.5 K, the highest measured temperature. Below T_2^F , ξ_1 continues to increase until T_1^F , so it is larger than ξ_2 at low temperatures. Meanwhile, the peak intensities show sudden jumps to their fully developed values just before T_1^F and T_2^F as well. Therefore, T_1^F , T_2^F , and T_3^F are defined as the temperatures that the q_1 , q_2 , and q_3 peaks are fully developed, respectively. Note that, between T_2^F and T_1^F , the q_1 peak intensity is low, indicating that the spin order is still fluctuating while the order corresponding to q_2 is already static. In addition, we find that ξ_3 is almost identical to ξ_2 . These tell how the orders corresponding to the three diffraction peaks evolve, which is discussed later.

To comprehensively elucidate the nature of the three resonant peaks at q_1 , q_2 , and q_3 , we plot in Fig. 3 the resonant profiles around the three q positions with $T = 20$ K, i.e., the scattering intensities as a function of reciprocal lattice $(0\ 0\ L)$, x-ray energy, and incident photon polarization. Since there is no polarization analyzer before

the detector, the polarizations of the scattered photons are not distinguished. That is, using a self-explanatory subscript convention, the detected scattered intensities for two different incident photon polarizations are

$$I_\pi = I_{\pi\pi} + I_{\pi\sigma}, \quad I_\sigma = I_{\sigma\pi} + I_{\sigma\sigma}.$$

Clearly, the resonant profiles of q_1 , q_2 , and q_3 are very different from each other in maximal intensity, resonant energy, and polarization dependence. For example, the resonant energies for the maximum peaks at q_1 , q_2 , and q_3 are 637 (π polarization), 648.2 (σ polarization), and 641.2 eV (π polarization), respectively. The maximal intensity at q_3 is about 23 times weaker than that at q_2 , and the maximal intensity for q_2 is about 30 times weaker than that of q_1 , based on the data of the resonance peaks taken with the same detector. The peak FWHM is generally independent of photon energy for all three resonance peaks (Fig. S6 in Supplemental Material [20]), indicating the observed diffractions are within the

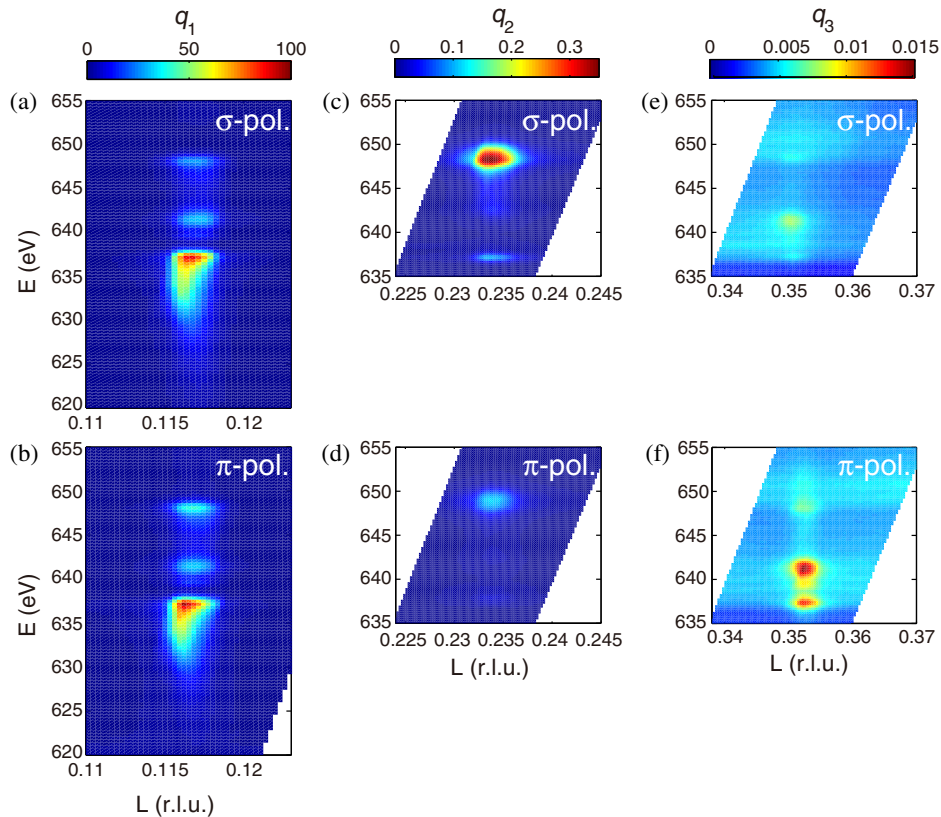


FIG. 3. Resonance profiles at q_1 , q_2 , and q_3 with $T = 20$ K. The resonance profiles at each resonance position are plotted as a function of the x-ray energy around the Mn L edge and reciprocal lattice vector $(0\ 0\ L)$, with σ (upper panels) or π (lower panels) linearly polarized incident photons. (a),(b) q_1 resonance profile. A photodiode detector is used to measure the scattering intensities I_σ and I_π , which are comparable in intensity. (c)–(f) q_2 and q_3 resonance profiles measured by a channeltron detector, due to their relatively weak intensity. For q_2 , the I_σ maximum is about 3 times the I_π maximum. For q_3 , the I_σ maximum is about 80% of the I_π maximum. The profiles in (a)–(f) cover the whole resonance energy range at the Mn L edge. All data shown here are raw scattering intensity without background subtraction or absorption correction. The color bars indicates the scattering intensity in arbitrary units.

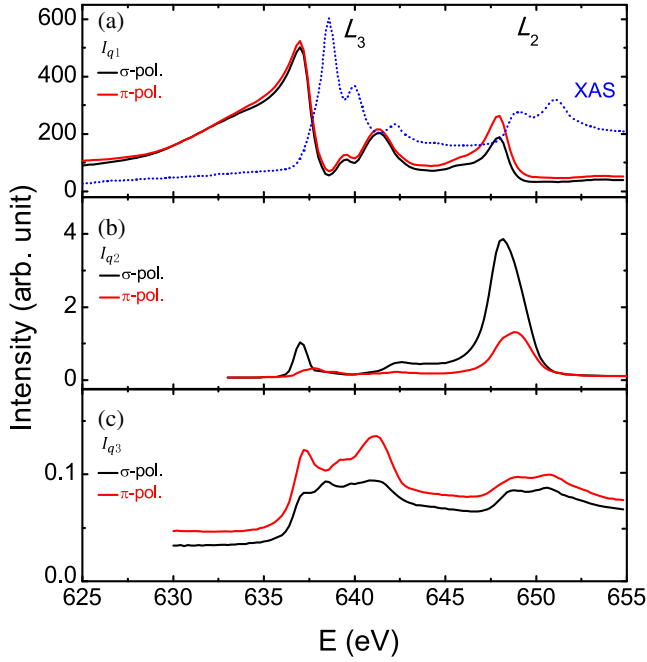


FIG. 4. q -integrated intensity I_q of the three resonance peaks shown in Fig. 3. (a) I_{q_1} with σ (black line) and π (red line) polarizations. I_{q_2} and I_{q_3} are plotted in (b) and (c), respectively.

kinematical approximation and FWHM is limited only by the correlation length of electronic orders.

The q -integrated resonant profiles are compared in Fig. 4, as a function of the energy and polarization. The XAS line shape is represented by the blue dashed line in Fig. 4(a). The difference between the XAS and RSXS peak positions originates from the fact that RSXS intensity is proportional to the square of the absolute value of the total scattering length, while XAS is proportional to the imaginary part of the total scattering length [15]. The resonant profile of the q_1 peak behaves similarly in both polarizations, consistent with its origin in resonant magnetic scattering. As illustrated by a simple analysis, magnetic scattering results in $\pi\pi$, $\pi\sigma$, and $\sigma\pi$ scatterings with comparable intensity [35,36]. The magnetic scattering matrix element is related to the dipole selection rules, which have the same origin as soft x-ray magnetic dichroism. This relation explains it having the strongest intensity among all three peaks. So the simple interpretation of q_1 peak is from helical magnetism. For the q_2 peak, I_σ is about triple I_π . Moreover, the energy positions of the q_2 profile differ between the σ and π polarizations, which is unlikely from magnetic scattering. The resonance profile of the q_3 peak shows moderate polarization dependence.

The different temperature, polarization, and photon energy dependencies of the q_1 , q_2 , and q_3 peaks indicate that q_2 and q_3 peaks are not merely the high harmonic peaks of q_1 . For example, the saturation of the q_1 peak intensity below T_1^F represents the full development of the incommensurate helical spin density wave. Remarkably,

the weak q_2 peak is fully developed slightly above T_1^F , when the q_1 peak intensity is still 2 orders of magnitude smaller than its full value. It implies that this is not a simple second-order harmonic of the spin density wave but an indication of another order which is induced by magnetic fluctuations. Applying the Landau theory to the phase transition and using a general symmetry analysis, we extract the nature of these orders by assuming that the Landau free-energy functional depends only on the fundamental Fourier components of the two different electronic orders. The q_1 peak corresponds to the double-helical spin density wave, $\vec{S}_{q_1,a} \propto (i, 1, 0)$, where $a = 1, 2$ denote the two helices. As $q_2 \approx 2q_1$, its order Π_{q_2} must be coupled to a quadratic term of \vec{S}_{q_1} . If we take Π_{q_2} to be a scalar, a natural choice of Π_{q_2} is the charge density wave ρ_{q_2} . The lowest-order coupling in the Landau theory can be written as

$$H_c = \sum_{ab} \lambda_{c,ab} \rho_{q_2} (\vec{S}_{q_1,a}^* \cdot \vec{S}_{q_1,b}^*) + \text{H.c.} \quad (1)$$

However, such an unequal charge distribution at different Mn sites could not be found in our local-density approximation calculations shown in Supplemental Material [20]. Instead, an orbital distribution with half the periodicity of the magnetic order can be explicitly obtained in the calculation. Moreover, there is no obvious charge or orbital order of the same period as the magnetic order in our calculation, which is consistent with our assignment of the q_1 peak as solely from the helical spin order. One certainly cannot absolutely rule out the contributions from other orders to q_1 , unless a resonance profile can be computed in a full calculation and compared with the experiments. This calculation is beyond the scope of this paper, however, based on our current calculations, and the observed polarization and temperature dependencies, the spin order should dominate the q_1 peak.

Here, we suggest that the order corresponding to q_2 is an ODW, which can be induced by the orbital redistribution in developing the double-helical spin density wave. In a simple helically ordered state, it is well known that an orbital redistribution can be induced by spin-orbital coupling in the presence of the crystal field, and such an orbital redistribution depends only on $|\vec{S}_{q_1}|$ [37], giving the x-ray magnetic linear dichroism effect. In this case, spin-parallel and -antiparallel Mn atoms have identical orbital (wave function) distribution, which explains why q_2 corresponds to an order with a period half that of the magnetic peak. This situation resembles the stripes in cuprates, but in MnP both orders are incommensurate with respect to the lattice. Since we observe resonance at the Mn $2p$ to $3d$ transition, Π_{ODW} could be attributed to an orbital order of $3d$ electrons, which is simultaneously developed in the helical spin state.

In certain multiferroic helimagnets, such as $\text{Ba}_3\text{NbFe}_3\text{Si}_2\text{O}_{14}$ and $\text{Ba}_3\text{TaFe}_3\text{Si}_2\text{O}_{14}$, diffractions from

local electronic density distortions are also observed at higher harmonics [38,39]. In these insulators with strong electron-phonon coupling, the charge distortions are usually induced by a large lattice distortion. However, different from the ionic insulating multiferroics, MnP is a metallic system where electron-phonon coupling is weakened by screening. So lattice distortion should not be the driving force behind the diffraction peaks observed in RSXS; otherwise, they would have similar resonance profiles. Thus, the ODWs discovered in MnP, which are also local electronic density distortions, should be the likely cause of the tiny lattice distortion found by neutron scattering [34], not the consequence. Consistently, our calculation shows an obvious charge redistribution in MnP without the need of a lattice distortion (part 4 in Supplemental Material [20]).

Now, in the case of *double-helical* spin order, we argue that a tiny orbital modulation can be induced by spin fluctuations even before the static helical spin order is developed. In general, the coupling between the ODW and the double-helical spin order in the Landau theory can be written as

$$H_Q = \sum_{\alpha} \Pi_{\alpha\alpha q_2} \left[\lambda_{Q,1}^{\alpha} ((S_{q_1,1}^{\alpha*})^2 + (S_{q_1,2}^{\alpha*})^2) + 2\lambda_{Q,2}^{\alpha} S_{q_1,1}^{\alpha*} S_{q_1,2}^{\alpha*} \right] + \text{H.c.} \quad (2)$$

With this coupling, there is a new phase in which $\langle S_{q_1,a}^{\alpha*} \rangle = 0$ but $\langle S_{q_1,1}^{\alpha*} S_{q_1,2}^{\alpha*} \rangle \neq 0$, which describes the locking of the magnetic fluctuations between the two helices. In general, this phase could exist slightly above T_s , thus explaining the intriguing full development of the q_2 peak at a slightly higher temperature than the q_1 peak. The linear coupling between the ODW and $S_{q_1,1}^{\alpha*} S_{q_1,2}^{\alpha*}$ must result in $\langle \Pi_{\alpha\alpha q_2} \rangle \neq 0$ if $\langle S_{q_1,1}^{\alpha*} S_{q_1,2}^{\alpha*} \rangle \neq 0$. This argument is generally known as “order by disorder” and has been used to explain the nematicity in FeAs-based superconductors in which a similar phenomenon has been observed in the parent compounds, e.g., BaFe₂As₂ [10,11], where the nematic orbital order emerges at a slightly higher temperature than the collinear spin order due to spin fluctuations.

Since the spins lie in the ab plane in the double-helical phase, the orbital moment should also be in the ab plane from the coupling H_Q . This result explains the observed polarization dependence of the q_2 peak and also suggests that the charge redistribution mainly occurs in the $d_{x^2-y^2}$ and d_{xy} orbitals (the orbital basis in the octahedral coordination with these two orbitals in the ab plane is used here for the ease of explanation, while we note Mn ions are in a tilted and distorted octahedrons made of P ions). The observation of the weak q_3 peak also lends strong support to the presence of an ODW order, since it represents the harmonics generated by the coupling between the ODW and the helical spin order.

The intensity of the q_3 peak is less than 1/600 of that of the SDW peak, yet it saturates at a slightly higher temperature. This remarkable behavior suggests that the q_3 peak is also nonmagnetic in nature. Moreover, since it is slightly stronger for π -polarized than σ -polarized incident photons [Fig. 4(c)], it should involve d_{xz} , d_{yz} , and possibly $d_{3z^2-r^2}$ orbitals. The simplest possibility for the q_3 peak would be the rearrangement or modulation of these orbitals induced by the coupling between the ODW (q_2) and the helical SDW (q_1) as a third-order effect. This possibility represents another unique ODW that is observed here for the first time.

In Figs. 5(a)–5(c), we summarize the observed orders. The helical spin density wave is shown in Fig. 5(a), represented by spins rotated by equally spaced in-plane angles. In Fig. 5(b), the in-plane ODW follows the SDW

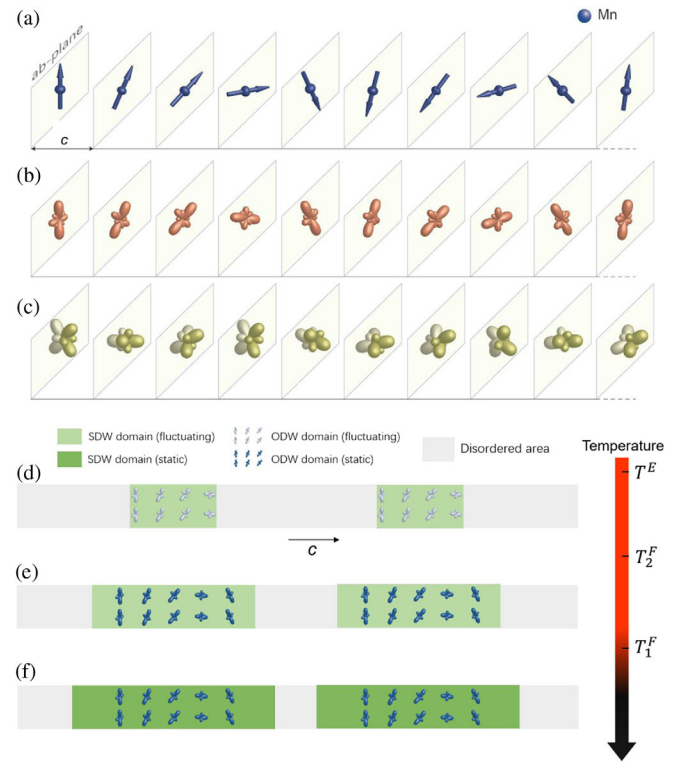


FIG. 5. An illustration of the intertwined orders in MnP. (a) The helical spin density wave with a period of about $8.6c$ is shown with Mn ions with equal spacing in the c direction. (b) The orbital density wave with $1/2$ the period is represented by an exaggerated mixture of d_{xy} and $d_{x^2-y^2}$ orbitals that rotates together with the spin but is symmetric under 180° rotation. (c) The orbital density wave with $1/3$ the period is represented by an exaggerated mixture of d_{xz} and d_{yz} orbitals that rotates 3 times as fast as the spin. (d) Cartoon showing that short-ranged and fluctuating SDW (represented by the blue area) and ODW domains (represented by the texture) share the same region in MnP for $T^E \geq T \geq T_2^F$. (e) When $T_2^F \geq T \geq T_1^F$, the ODW is fully developed and stops growing with a decreased temperature, while SDW domains continue to grow. There are regions with fluctuating spin order but without orbital order. (f) When $T \leq T_1^F$, the spin order is fully developed.

with half the period, represented by a charge distribution whose axis follows the orientation of the spin. In Fig. 5(c), the out-of-plane ODW rotates with one-third of the SDW period. These helical orbital density waves in MnP are discovered for the first time by RSXS, and they are intertwined with the helical spin density wave. It is particularly noteworthy that the temperature dependencies in Fig. 2 further illustrate the intricate relation between the spin and orbital orders. The short-ranged and fluctuating orbital and spin orders share the same domain as they both emerge and grow upon lowering the temperature [Fig. 5(d)]. This process starts from quite high temperatures, likely related to strain distributions in the system. Upon further cooling, as shown in Fig. 5(e), the ODW order freezes, and its domains are fixed after passing its fully developed temperature T_2^F . Meanwhile, the spin order is still fluctuating, and its domains keep expanding, since the intensity of the spin order peak is still a few percent of its full value at a low temperature. As a result, there are regions with fluctuating spin order but no orbital order in this temperature range. Because the orbital order is fairly weak, as shown by the weak diffraction peak intensity, the orbital distribution can be influenced or pinned by local strain or defects. Therefore, the orbitals in these regions are disordered, and its configuration could not follow the helical spin rotation. When the temperature is further lowered below T_1^F , the spin order is fully developed and its domains stop growing, as illustrated in Fig. 5(f). We note that, because the out-of-plane ODW in Fig. 5(c) is the descendant of the SDW and the in-plane ODW, its domain is identical to that of the in-plane ODW.

A similar observation is made in $\text{Pr}_{0.6}\text{Ca}_{0.4}\text{MnO}_3$, whose spin order correlation length is longer than its charge or orbital order correlation length, which is attributed to likely decoupling between spin and charge or orbital orders [40]. The diffraction peak intensity of its orbital order is also much weaker than the spin order in $\text{Pr}_{0.6}\text{Ca}_{0.4}\text{MnO}_3$, although its spin ordering temperature is lower than that of the charge or orbital order. So the picture revealed in Figs. 5(d)–5(f) through our detailed temperature dependence is likely ubiquitous for systems with both spin and orbital ordering, which explains the difference in the correlation lengths in $\text{Pr}_{0.6}\text{Ca}_{0.4}\text{MnO}_3$.

Our findings provide a comprehensive picture on the intricate interplay between spin and orbital orders in MnP and show that intertwined ordering is ubiquitous to the phase diagrams of unconventional superconductors, even in the case of low symmetry and incommensurate ordering. The extraordinary helical ODWs found here may provide a foundation for understanding the complex behaviors of spin and orbital order in helimagnets and correlated systems, in general, and for understanding the unconventional superconductivity in MnP and other related materials.

We acknowledge fruitful discussions with Professor J. L. Luo. This work is supported in part by the National Key

Research and Development Program of China (Grants No. 2016YFA0300200 and No. 2017YFA0303104), the National Natural Science Foundation of China (Grant No. 11804137), the Science and Technology Commission of Shanghai Municipality (Grant No. 15ZR1402900), and the Natural Science Foundation of Shandong Province (Grant No. ZR2018BA026). The experiments were conducted at beam line 13-3 of Stanford Synchrotron Radiation Lightsource (SSRL); SSRL is operated by the U.S. DOE Office of Basic Energy Science. Part of the research described in this paper was performed at the REIXS beam line of the Canadian Light Source (CLS) under Proposal No. 24-7906; CLS is supported by the Canada Foundation for Innovation, Natural Sciences and Engineering Research Council of Canada, the University of Saskatchewan, the Government of Saskatchewan, Western Economic Diversification Canada, the National Research Council Canada, and the Canadian Institutes of Health Research.

-
- [1] E. Fradkin, S. A. Kivelson, M. J. Lawler, J. P. Eisenstein, and A. P. Mackenzie, *Nematic Fermi Fluids in Condensed Matter Physics*, *Annu. Rev. Condens. Matter Phys.* **1**, 153 (2010).
 - [2] A. J. Achkar, M. Zwiebler, C. McMahan, F. He, R. Sutarto, I. Djianto, Z. Hao, M. J. P. Gingras, M. Hücker, G. D. Gu, A. Revcolevschi, H. Zhang, Y.-J. Kim, J. Geck, and D. G. Hawthorn, *Nematicity in Stripe-Ordered Cuprates Probed via Resonant X-Ray Scattering*, *Science* **351**, 576 (2016).
 - [3] M. Tsuchiizu, Y. Yamakawa, and H. Kontani, *p-Orbital Density Wave with d Symmetry in High-Tc Cuprate Superconductors Predicted by Renormalization-Group+Constrained RPA Theory*, *Phys. Rev. B* **93**, 155148 (2016).
 - [4] Y. Yamakawa, S. Onari, and H. Kontani, *Nematicity and Magnetism in FeSe and Other Families of Fe-Based Superconductors*, *Phys. Rev. X* **6**, 021032 (2016).
 - [5] H. Kontani and S. Onari, *Orbital-Fluctuation-Mediated Superconductivity in Iron Pnictides: Analysis of the Five-Orbital Hubbard-Holstein Model*, *Phys. Rev. Lett.* **104**, 157001 (2010).
 - [6] K. Kuroki, S. Onari, R. Arita, H. Usui, Y. Tanaka, H. Kontani, and H. Aoki, *Unconventional Pairing Originating from the Disconnected Fermi Surfaces of Superconducting $\text{LaFeAsO}_{1-x}\text{F}_x$* , *Phys. Rev. Lett.* **101**, 087004 (2008).
 - [7] Y. Shiomi, S. Iguchi, and Y. Tokura, *Emergence of Topological Hall Effect from Fanlike Spin Structure as Modified by Dzyaloshinsky-Moriya Interaction in MnP*, *Phys. Rev. B* **86**, 180404(R) (2012).
 - [8] J.-G. Cheng, K. Matsubayashi, W. Wu, J. P. Sun, F. K. Lin, J. L. Luo, and Y. Uwatoko, *Pressure Induced Superconductivity on the Border of Magnetic Order in MnP*, *Phys. Rev. Lett.* **114**, 117001 (2015).
 - [9] L. X. Yang, B. P. Xie, Y. Zhang, C. He, Q. Q. Ge, X. F. Wang, X. H. Chen, M. Arita, J. Jiang, K. Shimada, M. Taniguchi, I. Vobornik, G. Rossi, J. P. Hu, D. H. Lu, Z. X. Shen, Z. Y. Lu, and D. L. Feng, *Surface and Bulk Electronic Structures of LaFeAsO Studied by Angle-Resolved Photoemission Spectroscopy*, *Phys. Rev. B* **82**, 104519 (2010).

- [10] J.-H. Chu, J. G. Analytis, K. De Greve, P. L. McMahon, Z. Islam, Y. Yamamoto, and I. R. Fisher, *In-Plane Resistivity Anisotropy in an Underdoped Iron Arsenide Superconductor*, *Science* **329**, 824 (2010).
- [11] M. Yi, D. Lu, J.-H. Chu, J. G. Analytis, A. P. Sorini, A. F. Kemper, B. Moritz, S.-K. Mo, R. G. Moore, M. Hashimoto, W.-S. Lee, Z. Hussain, T. P. Devereaux, I. R. Fisher, and Z.-X. Shen, *Symmetry-Breaking Orbital Anisotropy Observed for Detwinned $\text{Ba}(\text{Fe}_{1-x}\text{Co}_x)_2\text{As}_2$ above the Spin Density Wave Transition*, *Proc. Natl. Acad. Sci. U.S.A.* **108**, 6878 (2011).
- [12] J. M. Tranquada, B. J. Sternlieb, J. D. Axe, Y. Nakamura, and S. Uchida, *Evidence for Stripe Correlations of Spins and Holes in Copper Oxide Superconductors*, *Nature (London)* **375**, 561 (1995).
- [13] T. P. Croft, C. Lester, M. S. Senn, A. Bombardi, and S. M. Hayden, *Charge Density Wave Fluctuations in $\text{La}_{2-x}\text{Sr}_x\text{CuO}_4$ and Their Competition with Superconductivity*, *Phys. Rev. B* **89**, 224513 (2014).
- [14] R. Qiao, T. Chin, S. J. Harris, S. Yan, and W. Yang, *Spectroscopic Fingerprints of Valence and Spin States in Manganese Oxides and Fluorides*, *Curr. Appl. Phys.* **13**, 544 (2013).
- [15] J. Fink, E. Schierle, E. Weschke, and J. Geck, *Resonant Elastic Soft X-Ray Scattering*, *Rep. Prog. Phys.* **76**, 056502 (2013).
- [16] P. Abbamonte, G. Blumberg, A. Rusydi, A. Gozar, P. G. Evans, T. Siegrist, L. Venema, H. Eisaki, E. D. Isaacs, and G. A. Sawatzky, *Crystallization of Charge Holes in the Spin Ladder of $\text{Sr}_{14}\text{Cu}_{24}\text{O}_{41}$* , *Nature (London)* **431**, 1078 (2004).
- [17] P. Abbamonte, A. Rusydi, S. Smadici, G. D. Gu, G. A. Sawatzky, and D. L. Feng, *Spatially Modulated "Mottness" in $\text{La}_{2-x}\text{Ba}_x\text{CuO}_4$* , *Nat. Phys.* **1**, 155 (2005).
- [18] F. M. F. de Groot, J. C. Fuggle, B. T. Thole, and G. A. Sawatzky, *2p x-ray Absorption of 3d Transition-Metal Compounds: An Atomic Multiplet Description Including the Crystal Field*, *Phys. Rev. B* **42**, 5459 (1990).
- [19] S. P. Cramer, F. M. F. de Groot, Y. Ma, C. T. Chen, F. Sette, C. A. Kipke, D. M. Eichhorn, K. Chan, W. H. Armstrong, E. Libby, G. Christou, S. Brooker, V. McKee, O. C. Mullins, and J. C. Fuggle, *Ligand Field Strengths and Oxidation States from Manganese L-Edge Spectroscopy*, *J. Am. Chem. Soc.* **113**, 7937 (1991).
- [20] See Supplemental Material at <http://link.aps.org/supplemental/10.1103/PhysRevX.9.021055> for more information about sample characterization, RSXS experiment setup, theoretical calculation, and additional data.
- [21] W. Tremel, R. Hoffmann, and J. Silvestre, *Transitions between NiAs and MnP Type Phases: An Electronically Driven Distortion of Triangular Nets*, *J. Am. Chem. Soc.* **108**, 5174 (1986).
- [22] Y. Xu, M. Liu, P. Zheng, X. Chen, J.-g. Cheng, J. Luo, W. Xie, and Y.-f. Yang, *First-Principles Calculations of the Magnetic and Electronic Structures of MnP under Pressure*, *J. Phys. Condens. Matter* **29**, 244001 (2017).
- [23] E. E. J. Huber and H. D. Ridgley, *Magnetic Properties of a Single Crystal of Manganese Phosphide*, *Phys. Rev.* **135**, A1033 (1964).
- [24] J. W. Simonson, Z. P. Yin, M. Pezzoli, J. Guo, J. Liu, K. Post, A. Efimenko, N. Hollmann, Z. Hu, H.-J. Lin, C.-T. Chen, C. Marques, V. Leyva, G. Smith, J. W. Lynn, L. L. Sun, G. Kotliar, D. N. Basov, L. H. Tjeng, and M. C. Aronson, *From Antiferromagnetic Insulator to Correlated Metal in Pressurized and Doped LaMnPO* , *Proc. Natl. Acad. Sci. U.S.A.* **109**, E1815 (2012).
- [25] D. E. McNally, J. W. Simonson, K. W. Post, Z. P. Yin, M. Pezzoli, G. J. Smith, V. Leyva, C. Marques, L. DeBeer-Schmitt, A. I. Kolesnikov, Y. Zhao, J. W. Lynn, D. N. Basov, G. Kotliar, and M. C. Aronson, *Origin of the Charge Gap in LaMnPO* , *Phys. Rev. B* **90**, 180403(R) (2014).
- [26] C. de la Cruz, Q. Huang, J. W. Lynn, J. Li, W. Ratcliff II, J. L. Zarestky, H. A. Mook, G. F. Chen, J. L. Luo, N. L. Wang, and P. Dai, *Magnetic Order Close to Superconductivity in the Iron-Based Layered $\text{LaO}_{1-x}\text{F}_x\text{FeAs}$ Systems*, *Nature (London)* **453**, 899 (2008).
- [27] P. C. Dai, *Antiferromagnetic Order and Spin Dynamics in Iron-Based Superconductors*, *Rev. Mod. Phys.* **87**, 855 (2015).
- [28] J. Y. Kim, T. Y. Koo, and J. H. Park, *Orbital and Bonding Anisotropy in a Half-Filled GaFeO_3 Magnetoelectric Ferrimagnet*, *Phys. Rev. Lett.* **96**, 047205 (2006).
- [29] H. Jang, G. Kerr, J. S. Lim, C.-H. Yang, C.-C. Kao, and J.-S. Lee, *Orbital Reconstruction in a Self-Assembled Oxygen Vacancy Nanostructure*, *Sci. Rep.* **5**, 12402 (2015).
- [30] G. P. Felcher, *Magnetic Structure of MnP*, *J. Appl. Phys.* **37**, 1056 (1966).
- [31] J. B. Forsyth, S. J. Pickart, and P. J. Brown, *The Structure of the Metamagnetic Phase of MnP*, *Proc. Phys. Soc.* **88**, 333 (1966).
- [32] T. Yamazaki, *Novel Phenomena Caused by the Chiral Orders in Metallic Magnets*, *Doctoral dissertation*, Kyoto University, 2010.
- [33] R. M. Moon, *Neutron Polarization Analysis Measurements on the Spiral Phase of MnP*, *J. Appl. Phys.* **53**, 1956 (1982).
- [34] S.-i. Yano, D. Lançon, H. M. Rønnow, T. C. Hansen, E. Ressouche, N. Qureshi, B. Ouladdiaf, and J. S. Gardner, *Suppression of Magnetic Order before the Superconducting Dome in MnP*, *J. Phys. Soc. Jpn.* **87**, 023703 (2018).
- [35] H. Jang, B. Y. Kang, B. K. Cho, M. Hashimoto, D. Lu, C. A. Burns, C.-C. Kao, and J.-S. Lee, *Observation of Orbital Order in the Half-Filled 4f Gd Compound*, *Phys. Rev. Lett.* **117**, 216404 (2016).
- [36] S. W. Lovesey and S. P. Collins, *X-Ray Scattering and Absorption by Magnetic Materials* (Clarendon, Oxford, 1996).
- [37] J. Stöhr and H. C. Siegmann, *Magnetism: From Fundamentals to Nanoscale Dynamics* (Springer, New York, 2006).
- [38] V. Scagnoli, S. W. Huang, M. Garganourakis, R. A. de Souza, U. Staub, V. Simonet, P. Lejay, and R. Ballou, *Dzyaloshinskii-Moriya Driven Helical-Butterfly Structure in $\text{Ba}_3\text{NbFe}_3\text{Si}_2\text{O}_{14}$* , *Phys. Rev. B* **88**, 104417 (2013).
- [39] M. Ramakrishnan, Y. Joly, Y. W. Windsor, L. Rettig, A. Alberca, E. M. Bothschafter, P. Lejay, R. Ballou, V. Simonet, V. Scagnoli, and U. Staub, *Crystal Symmetry Lowering in Chiral Multiferroic $\text{Ba}_3\text{TaFe}_3\text{Si}_2\text{O}_{14}$ Observed by X-Ray Magnetic Scattering*, *Phys. Rev. B* **95**, 205145 (2017).
- [40] K. J. Thomas, J. P. Hill, S. Grenier, Y.-J. Kim, P. Abbamonte, L. Venema, A. Rusydi, Y. Tomioka, Y. Tokura, D. F. McMorrow, G. Sawatzky, and M. van Veenendaal, *Soft X-Ray Resonant Diffraction Study of Magnetic and Orbital Correlations in a Manganite Near Half Doping*, *Phys. Rev. Lett.* **92**, 237204 (2004).